

Enhancing numerical accuracy in the prediction of rotor wake vortex structures

Cite as: Phys. Fluids **36**, 037137 (2024); doi: [10.1063/5.0196010](https://doi.org/10.1063/5.0196010)

Submitted: 4 January 2024 · Accepted: 25 February 2024 ·

Published Online: 13 March 2024



View Online



Export Citation



CrossMark

Andrew Bodling,^{1,a)} Clemens Schwarz,² C. Christian Wolf,² and Anthony D. Gardner²

AFFILIATIONS

¹Science and Technology Corporation, Moffett Field, California, USA

²German Aerospace Center (DLR), Göttingen, Germany

Note: Presented at the VFS International 79th Annual Forum & Technology Display, West Palm Beach, FL, USA, May 16-18, 2023.

^{a)}Author to whom correspondence should be addressed: andrewbodling@gmail.com

ABSTRACT

In modern high-fidelity computational fluid dynamic simulations, the primary vortex system in hover often breaks down into secondary vortices. The sources of numerical error influencing the prediction of the vortex system were studied by performing high-fidelity simulations of the wake of a two-bladed rotor and comparing the predictions to stereoscopic particle image velocimetry measurements in different measurement planes. Various numerical inputs, including sub-iteration convergence, blade pitch offset, and grid resolution, were varied to resolve discrepancies between the measured and predicted vortex characteristics from a previous study done by the authors. A parametric study on near- and off-body solver sub-iteration convergence demonstrated that although the secondary vortex characteristics converged as the sub-iteration convergence of both solvers increased, a large discrepancy in the number of secondary vortices remained. This discrepancy was investigated by varying the thrust, where it was found that the breakdown of the primary vortex is directly linked to the number of secondary vortices. Dissimilarities in the blade pitch angle, which could not be avoided in the experiment, were modeled by intentionally using an offset in the blade pitch angle of the two blades. It was shown that as blade pitch angle offset increases, vortex pairing becomes more distinct. When vortex pairing occurred in both the experiment and simulation, the decay of secondary vortices in the experiment and simulation agreed best. To better match the experimental resolution, grid resolution was increased and comparing the two simulations, the finer mesh simulation agreed best with the measured primary and secondary vortex characteristics.

Published by AIP Publishing. <https://doi.org/10.1063/5.0196010>

NOMENCLATURE

| | | | |
|-----------------|--|-------------------|--|
| c_b | Mid-span blade chord length, $c_b = 0.061\text{ m}$ | R | Rotor radius, $R = 0.775\text{ m}$ |
| c | Chord length at the blade tip, $c = 0.042\text{ m}$ | T | Rotor thrust (N) |
| C_T | Thrust coefficient, $C_T = T/(\rho\pi\Omega^2 R^4)$ | u, v, w | Velocities in x , y , and z directions (m/s) |
| k | Normalized turbulent kinetic energy | U_∞ | Free stream velocity, m/s |
| k_x, k_y, k_z | Cartesian components of k | V_h | Hover-induced velocity, $V_h = V_{\text{tip}}\sqrt{\frac{C_T}{2}}$ (m/s) |
| k_{yz} | Component of k in the y - z plane | V_{tip} | Rotor tip speed, $V_{\text{tip}} = \Omega R = 101.76\text{ m/s}$ |
| N_b | Number of blades, $N_b = 2$ | V_{yz} | Velocity in the y - z plane |
| NB | Near-body | $V_{\Theta,\max}$ | Maximum swirl velocity (m/s) |
| OB | Off-body | x, y, z | Coordinates in the reference frame (m) |
| OOM | Order of magnitude | Γ | Circulation (m^2/s) |
| Q | Q-criterion, Eq. (1) ($1/\text{s}^2$) | ρ | Air density (kg/m^3) |
| \hat{Q} | Non-dimensional Q-criterion | σ | Rotor solidity, $\sigma = N_b c / \pi R = 0.05$ |
| Q_s | Signed Q-criterion, $Q_s = Q \cdot \frac{\omega_z}{ \omega_z }$ ($1/\text{s}^2$) | Ψ_w | Rotor wake age (= 0° when blade parallel with y axis) |
| r | Radial coordinate (m) | ω | Vorticity (1/s) |
| | | ω_z | Vorticity normal to x , y plane (1/s) |
| | | Ω | Angular velocity of the rotor, $\Omega = 131.3\text{ rad/s}$ |

I. INTRODUCTION

The understanding of the complex spatiotemporal development of rotor flows is still a major challenge for both state-of-the-art experimental and numerical techniques, with recent studies focusing on the phenomenon of wake breakdown and its effect on the rotor performance. Chaderjian and Buning¹ first observed smaller secondary vortex structures between the blade tip vortices (see Fig. 1), which were termed “worms” and in a review of hover prediction workshops Egolf *et al.*² noted secondary vortex braids and wake breakdown as an important open question due to the wake’s high impact on the rotor performance predicted in simulations. As high-order methods and finer grids became the state-of-the-art,^{3,4} these structures became a frequently observed phenomenon in simulations. These structures may be both a genuine physical phenomenon and also a numerical artifact associated with inadequate convergence (see, e.g., Ref. 5). Other associated fields have also noted secondary vortices, for example, in corotating Kelvin–Helmholtz instabilities of mixing layers,⁶ or counterrotating von Kármán vortices in the wake of bluff bodies.⁷

Chaderjian contends that the secondary vortices are generated from the vorticity present in the blade shear layer that is perpendicular to the core of the vortex.⁸ The axial stretching occurs when a portion of the shear layer is drawn into the vortex created by the preceding blade tip. This, in turn, enhances the rotation of the vortices in worms, as a consequence of momentum conservation. Research conducted by Abras *et al.*⁴ revealed that the presence and characteristics of secondary vortices in computational fluid dynamics (CFD) rotor investigations significantly rely on factors such as simulation duration and the numerical configuration, encompassing mesh resolution and turbulence model. Recent computational analyses have also explored the impact of time marching on secondary vortex braids and wake breakdown,⁹ and they have examined volume rendering techniques to enhance comprehension of this phenomenon.¹⁰ Furthermore, proper orthogonal decomposition (POD) was employed to examine the wake breakdown.¹¹

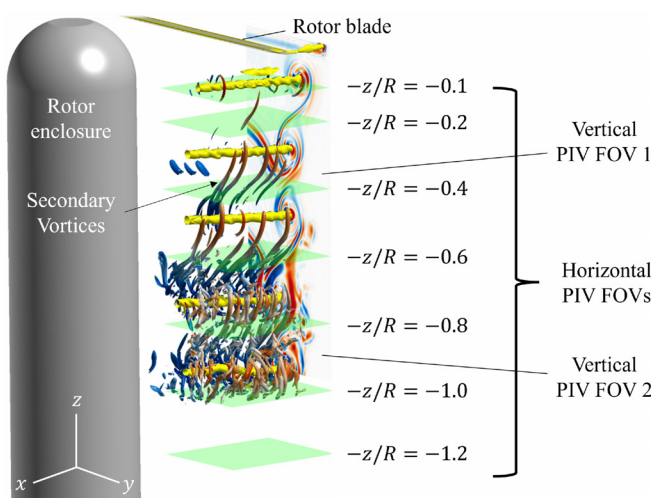


FIG. 1. Drawing illustrating rotor arrangement and PIV fields of view (FOV) with CFD data from the current study.

An overview of the state of the art by Chaderjian¹² notes that it is the current consensus that “These instabilities naturally occur outside the turbulent boundary layer as large eddy simulation (LES) resolved flow when using hybrid RANS (Reynolds Averaged Navier–Stokes)/LES turbulence models with adequate grid support.” Secondary vortices may generate additional noise and vibrations due to impingement on structures below the rotor and on the rotor itself due to the variable blockage of the wake. Therefore, it is important to understand how to consistently and accurately predict their presence.

Although there is a long history of helicopter wake measurement,^{13–15} most of those have been concerned with the characterization of the primary blade tip vortices. When detailed measurements have been made, it has been shown that good agreement with CFD is possible for computations, which are sufficiently finely discretized.^{16,17} On the other hand, there has been limited experimental evidence in previous research supporting the presence of secondary vortices. While Gray¹⁸ hinted at the presence of secondary vortices through smoke visualizations, concrete experimental confirmation of their existence was only presented recently in a volumetric flow measurement conducted by the current authors.¹⁹ This measurement was conducted in the wake of a two-bladed, heavily loaded model helicopter operating in ground effect. The tests in Ref. 19 were conducted using a time-resolved and volumetric variant of particle image velocimetry called the “Shake-the-Box” method. Later, Bodling and Potsdam²⁰ performed a detailed CREATE™-AV Helios CFD study of this test case, particularly focusing on the grid and sub-iteration convergence of the Spalart–Allmaras delayed detached eddy simulation (SA-DDES). They concluded that the secondary vortices are formed when the vortex sheets are entrained into the tip vortices and break apart into small coherent structures. They showed that as the near-body sub-iteration residual drop increases, the vortex sheet is broken down less, and correspondingly, both the rotor performance data and peak number of secondary vortices converge. A simplified vortex ring study was performed to observe how vortex breakdown is influenced by off-body grid structure and different levels of sub-iteration convergence. In agreement with the rotor case, when all flow solvers were sufficiently converged, vortex breakdown was minimized. Making direct comparisons to the data was challenging due to the relatively coarse discretization, and uncertainties linked to the experimental setup with a rather flexible full helicopter model in ground effect.

To solve these problems, an enhanced setup²¹ was designed using a new, stiffer rotor testing apparatus out-of-ground effect and with an axisymmetric support structure. The same rotor blades were used as previously, together with a high-speed stereoscopic particle image velocimetry (PIV) system measuring in planes. This offers superior in-plane spatial resolution in comparison to the previous volumetric measurements. This setup was computed using Helios, giving a greater understanding of the secondary vortex development, behavior, stability, and decay. The comparison between simulations and experiment showed good qualitative agreement between experiment and simulation as to the distribution of swirl velocity and circulation over the secondary structure size for larger secondary structures. However, for small scales, the match was poor, probably due to needing additional filtering of the data to match the resolution of PIV and CFD (see Ref. 22).

The goal of this study is to build on the previous investigation by Schwarz *et al.*²¹ and identify the sources of error that are causing the

discrepancies. The numerical inputs are varied to progressively increase the accuracy of the predicted primary and secondary vortex characteristics. We will investigate how well the predictions agree with the measurements once sub-iteration convergence is high enough. The relation between tip vortex breakdown and the number of secondary vortices is shown. Additionally, this study investigates what role vortex pairing has on the decay of the secondary vortices. Finally, the grid resolution is increased to observe how the predictions are affected as the simulation approaches the experimental resolution. Using the numerical setup that best agrees with the experiment, the solution will then be used to elucidate the development and decay of the secondary vortices.

II. EXPERIMENTAL AND NUMERICAL SETUP

A. Test rotor

A hover test-stand was operated at the German Aerospace Center (DLR) in Göttingen, Germany. The rotor plane is 4 rotor radii ($4R$) above the ground, with two untwisted and untapered “Spinblades Black Belt 685” rotor blades with chord $c_b = 0.061\text{ m}$ reducing to $c = 0.042\text{ m}$ at the parabolic tip. The blades use a 14.8% symmetric airfoil, which was scanned after coating with nonreflective paint to improve the PIV measurement. The room is $10 \times 12 \times 7\text{ m}^3$. The rotor thrust was measured using a piezoelectric balance and was set at 80% of the rotor’s maximum thrust to match Wolf *et al.*¹⁹ Additional values are in Table I.

B. Particle image velocimetry

The flow field below the rotor is measured with two groups of PIV planes, shown in Fig. 1. First, vertical planes were taken in two fields of view (FOV) with a final vector spacing of 0.77 mm to analyze the primary blade tip vortices. Second, horizontal planes were taken in seven layers spanning $z = -0.1R$ to $z = -1.2R$, with a final vector spacing of 0.46 mm . An acquisition rate of 945 double images per second, or 45 images per revolution was used, with 26 mJ per laser pulse and $\Delta t = 50\text{ }\mu\text{s}$ between image pairs. The planes were measured sequentially, moving the laser and recalibrating the cameras between each measurement. The seeding was aerosolized di-ethyl-hexyl-sebacate (DEHS) from 1.2 to $2.3\text{ }\mu\text{m}$ diameter. Both PIV cameras (Phantom VEO640L, detailed in Ref. 21) operate at a reduced resolution of 2176×1452 pixels and are equipped with lenses having focal lengths of 180 mm for the horizontal FOVs and 85 mm for the vertically oriented overview measurement planes. The particle images were evaluated using Davis 8.4 (by LaVision) using multi-grid cross

correlation with a final, round interrogation window size of 16 pixels and an interrogation window overlap of 75%.

C. Hot-wire anemometry

Constant temperature hot-wire anemometry provided turbulence statistics with a response time of approximately $10\text{ }\mu\text{s}$, nominally offering a bandwidth of 100 kHz and was sampled at 200 kHz . The single-sensor probe-type “TSI 1210-T1.5” was coupled with a “DISA 55M” anemometer unit. The probe was operated using the constant temperature anemometry (CTA) measurement principle in which the probe was heated up to a significantly higher temperature than the investigated fluid. The probe was oriented parallel to the x -axis and thus measured the absolute value of the instantaneous velocity component in the $y-z$ plane. Measurements were taken at 7 radial positions in the wake separated by $\Delta y/R = 0.05$, ranging from $y/R = 0.7$ to $y/R = 1.0$. Axially, the wake was sampled 34 locations separated by $\Delta z/R = 0.032$, ranging from $z/R = -0.0645$ to $z/R = -1.129$.

III. NUMERICAL SETUP

A. Numerical methodology

Helios version 12.2²³ is employed for the simulations, which is the rotary-wing product of the US Army Aviation & Missile Center and HPCMP CREATE™-AV (Air Vehicles) program sponsored by the DoD High Performance Computing Modernization Office. Helios utilizes an innovative approach employing multiple meshes and solvers for CFD. This method involves employing unstructured and/or structured meshes in the vicinity of solid surfaces (“near-body”) to accurately capture effects related to viscous interactions with walls. The latest Helios release incorporates various solvers for near-body simulations, such as the unstructured mesh solvers FUN3D and kCFD, the curvilinear structured mesh solver OVERFLOW, and the strand mesh solver mStrand. To model the wake, Cartesian grids are utilized in the “off-body” region, employing high-order algorithms and adaptive mesh refinement (AMR). The management of Cartesian meshes is executed through a block structured mesh system capable of adapting to geometry and solution characteristics. Furthermore, an overset procedure known as PUNDIT²⁴ facilitates data exchange and accommodates relative motion among moving meshes. A software integration framework, built using Python and characterized by its lightweight nature, manages and coordinates the simulation as well as the exchange of data among different modules.

Section II B outlines the primary Helios flow solver modules utilized in this investigation.

B. Flow solvers

1. FUN3D

FUN3D 13.5²⁵ is a near-body unstructured grid flow solver, continuously developed by NASA. It operates as a node-centered, finite-volume solver capable of solving both the unsteady Reynolds Averaged Navier-Stokes (URANS) and hybrid RANS/LES equations. Employing a Roe upwind scheme, it achieves second-order spatial accuracy. For time-accurate computations, it adopts an optimized, second-order backward difference (BDF2OPT) time stepping scheme in conjunction with dual-time stepping sub-iterations. Additionally, it incorporates the SA-DDES turbulence model, which includes Dacles–Mariani

TABLE I. Rotor data.

| Parameter | Value |
|--|--------------------------------------|
| Rotational frequency Ω | $131.3\text{ rad/s}; 20.9\text{ Hz}$ |
| Blade pitch | 10.4° |
| Rotor thrust | 112.8 N |
| Thrust coefficient $C_T = T/\rho\pi\Omega^2 R^4$ | 0.0048 |
| Air density ρ | 1.20 kg/m^3 |
| Blade loading C_T/σ | 0.096 |
| Induced velocity in hover V_h | 4.98 m/s |

rotation correction and provisions for handling negative turbulence variables.^{26–28}

2. OVERFLOW

The near-body structured, curvilinear grid flow solver OVERFLOW 2.3b,²⁹ developed by NASA, functions as a node-centered, finite-difference solver that is capable of solving both the URANS and hybrid RANS/LES equations. A nominally spatially sixth-order accurate central difference scheme with sixth difference-based scalar artificial dissipation is chosen for this study. The amount of artificial dissipation is controlled by the dissipation coefficient DIS4 and the smoothing parameter SMOO, which changes how the spectral radius of the Jacobian matrix is computed. Based on previous numerical experiments, a value of DIS4 between 0.005 and 0.04 is recommended, where the DIS4 coefficient used should be kept as small as possible while still maintaining stability. With SMOO = 0.0, the spectral radius is computed as normally, $|U| + kc$. With SMOO = 1.0, the sound speed c is replaced by the local velocity scaled by the reference Mach number $\|V\|/M_{ref}$, which reduces smoothing in low-speed regions. Intermediate values of SMOO combine the effects of both the speed of sound and local velocity. More information about these parameters, including the form of the artificial dissipation operator, is given in Jespersen *et al.*³⁰ Time-accurate computations utilize an optimized, second-order, backward difference (BDF2OPT) time stepping scheme alongside dual-time stepping sub-iterations. Additionally, the SA-DDES turbulence model with the Dacles–Mariani rotation correction is applied.³¹

3. SAMCart

The off-body mesh system employs the Cartesian solver SAMCart.^{32,33} SAMCart handles the Euler or Navier–Stokes equations and employs a central difference spatial discretization scheme, ensuring fifth-order accuracy for inviscid terms and fourth-order accuracy for viscous terms. Its time integration scheme involves an implicit second-order BDF2 LU-SGS scheme. To effectively and automatically capture dynamic features in unsteady flow, SAMCart is capable of applying adaptive mesh refinement (AMR) based on appropriate adaptation criteria. However, in this study, the fixed refinement capability, which allows users to define rectangular areas with specific grid resolutions, is employed to comprehensively and uniformly capture blade wake sheets and tip vortices. Furthermore, the SA-DES turbulence model, augmented with Dacles–Mariani rotation correction, is incorporated. A summary of the flow solvers is shown in Table II.

C. Geometry modeling, meshing, and boundary conditions

The boundary conditions applied to the cylinder hub and rotor blades involve viscous adiabatic solid walls, specifically denoting a no-slip wall with extrapolation of density/pressure. At the boundaries far from the rotor, free stream conditions are implemented, incorporating an inviscid ground plane positioned $4R$ below the rotor. To prevent any potential boundary effects on the close-proximity solution, the far-field boundaries extend to a distance of $15R$ away from the blades in all directions. The experimental setup involves slight blade bending and coning, factors that are not considered in the simulations. Given the cylinder hub's capacity to adequately represent hub blockage

TABLE II. Summary of flow solvers.

| Flow solver | Attribute |
|-------------|--|
| FUN3D | Near-body solver Unstructured flow solver Second-order spatial accuracy Second-order time integration SA-DDES turbulence model |
| OVERFLOW | Near-body solver Structured, curvilinear flow solver Fifth-order spatial accuracy Second-order time integration SA-DDES turbulence model |
| SAMCart | Off-body solver Cartesian flow solver Fifth-order spatial accuracy Second-order time integration SA-DES turbulence model |

effects, the rotor geometry is truncated at $0.20R$, disregarding additional components like blade attachments and pitch links.

Figure 2 depicts the computational grid setup. The red boundaries represent the no-slip walls encompassing the cylinder hub and blades. Additionally, the green mesh illustrates the trimmed unstructured near-body mesh utilized for simulating the cylinder hub, a component solved using FUN3D. Throughout the cylinder grid, $y^+ < 1$. All FUN3D calculations use 10 sub-iterations, which on average achieves about 2.5 orders of magnitude (OOM) sub-iteration residual drop or an absolute residual of 12 OOM at the final sub-iteration. The residual drop is computed from the L_2 -norm of the mean flow residual and is not volume-scaled. The cyan mesh is the extents of the structured volume mesh that is used to model the rotor blades and is solved by OVERFLOW. The rotor blade grids consists of overlapping main blade, root cap, and tip cap meshes. Each blade, root cap, and tip cap mesh extend out 1.1 chords. The black mesh represents the off-body Cartesian mesh, which is resolved by SAMCart.

A single fixed refinement box is employed to capture the wake. The resolution of this fixed refinement box is varied in this paper to

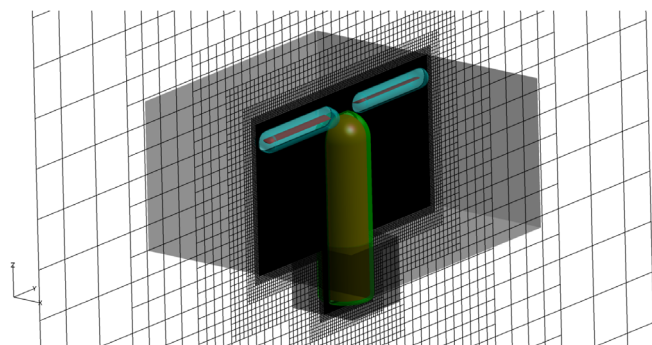


FIG. 2. Computational mesh with refinement box.

TABLE III. Number of grid points for main mesh components (without fringes).

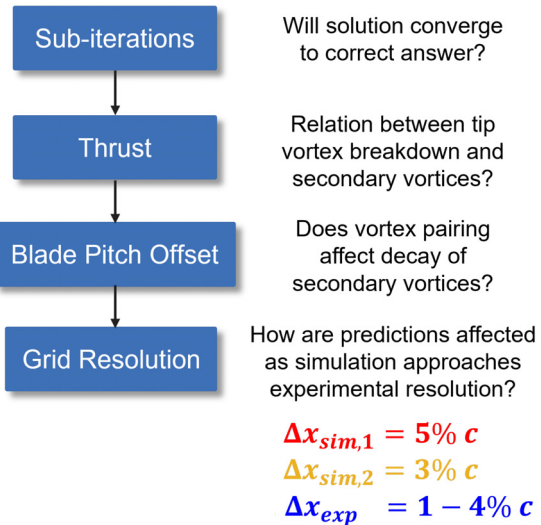
| Volume mesh | Number of grid points |
|---------------------------|-----------------------|
| Coarse cylinder hub | 1.9×10^6 |
| Fine cylinder hub | 3.6×10^6 |
| Coarse total blade | 10.6×10^6 |
| Fine total blade | 27.5×10^6 |
| Coarse main blade | 7.6×10^6 |
| Fine main blade | 22.4×10^6 |
| Coarse Cartesian off-body | 0.635×10^9 |
| Fine Cartesian off-body | 1.46×10^9 |

investigate the effects of grid resolution. A grid resolution of $\Delta x = \Delta y = \Delta z = 5\%c = 0.0021$ m and $\Delta x = \Delta y = \Delta z = 3\%c = 0.00126$ m is used, where c is the airfoil chord at the blade tip. The $5\%c$ resolution simulations extend to $z/R = -1.25$. Due to solver constraints, the $3\%c$ resolution simulations extend to $z/R = -1.0$. Beyond the fixed refinement box, the mesh undergoes gradual coarsening, reducing by a factor of two in all dimensions. A summary of the number of grid points for the main mesh components is shown in **Table III**, where “coarse” and “fine” refer to the simulations using an off-body fixed refinement box mesh spacing of $5\%c$ and $3\%c$, respectively. The chordwise \times spanwise \times normal dimensions of the “coarse” and “fine” mesh blade is $311 \times 241 \times 101$ and $423 \times 352 \times 151$ points, respectively. To ensure high-quality overset between the near and off-body grids, the outer boundary mesh spacing of the near-body volume meshes for the “coarse” and “fine” simulations is the same spacing as the respective off-body grid ($5\%c$ and $3\%c$). All cases presented in this manuscript are run with a time step size of $\Delta t = 0.25^\circ$. The “fine” mesh simulation with high sub-iterations (100 OVERFLOW and 27 SAMCART sub-iterations) took about 1.55×10^6 CPU hours to complete 21 revolutions.

IV. RESULTS

We start by using the numerical inputs used in the previous study done by Schwarz *et al.*²¹ with a fixed refinement box resolution of $\Delta x = \Delta y = \Delta z = 5\%c = 0.0021$ m, high numerical dissipation (0.04 artificial dissipation coefficient and 0.0 smoothing parameter), a blade pitch angle of $\beta = 10.4^\circ$, 50 near-body (OVERFLOW) sub-iterations, and 10 off-body (SAMCart) sub-iterations. Each case shown in this manuscript is run sufficiently long to let any initial startup transients to die out. After 10 revolutions, the figure of merit for each case changed less than 0.1%. All snapshots and time-averaging shown are after 16 revolutions, which is several revolutions after the integrated forces have become statistically steady.

Figure 3 shows an outline of the primary and secondary vortex analysis. We will first vary sub-iterations to see whether the solution converges to the correct answer. Then, the rotor thrust is varied to determine the relationship between the breakdown of the tip vortices and the secondary vortices. Next, the blade pitch offset is varied to see whether vortex pairing affects the decay of the secondary vortices. In the experiment, the grid resolution is approximately 1 to 4% of the chord, where 1% is the vector spacing and 4% is the interrogation window size. The grid resolution of the simulations will be increased from $5\%c$ to $3\%c$ to see how the predictions are affected as the simulation

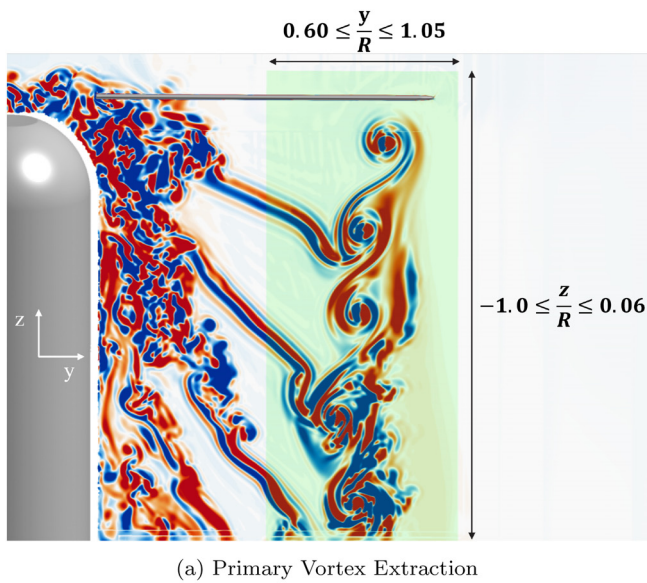
**FIG. 3.** Outline of primary and secondary vortex analysis.

approaches the range of the experimental resolution. Using the numerical setup that best agrees with the experiment, the solution will then be used to elucidate the development and decay of the secondary vortices.

In both the experiment and simulation, a vertical plane is extracted to characterize the primary vortices. This plane, which extends one radius below the radius, is illustrated in **Fig. 4(a)**. Also, in both the experiment and simulation, horizontal planes are extracted to characterize the secondary vortices. As shown in **Fig. 4(b)**, these planes extend from 0.1 to 1 radius below the rotor and in the radial direction from $r = 0.68R$ to $r = 1.01R$. The location and extents of the extraction planes were chosen so that both the development and decay of the primary and secondary vortices could be characterized. The number of secondary vortices at each axial position is quantified using the vortex identification scheme from Schwarz *et al.*²¹ For a given horizontal slice, the Q-criterion is applied to the velocity fields. Q is calculated by employing a two-dimensional velocity gradient tensor using the velocity components within the plane (u, v), as detailed in the methodology outlined by Chen and colleagues in their work,³⁴ presented as

$$Q = \frac{\partial u}{\partial x} \frac{\partial v}{\partial y} - \frac{\partial u}{\partial y} \frac{\partial v}{\partial x} - \frac{1}{2} \left(\frac{\partial u}{\partial x} + \frac{\partial v}{\partial y} \right)^2. \quad (1)$$

The Q values are obtained from velocity fields that undergo post-processing using a two-dimensional (2D) median filter (a filter that substitutes each value with the median of its neighboring values) with dimensions of 5.04 mm (equal to $4\Delta x$ and $4\Delta y$) in both spatial directions. This filtering process aims to reduce noise interference. Only regions surpassing a threshold of $Q = 10^5 \cdot \frac{1}{s^2}$ are considered, while all lower values are set to zero. Moreover, the MATLAB function “bwpropfilt,” illustrated in **Fig. 5**, is employed to exclusively identify connected areas surpassing the Q-threshold, ensuring they possess a minimum minor axis length of 4.12 mm. The minor axis length specifies the length of the minor axis of the equivalent ellipse that has the same normalized second central moments as the region.



(a) Primary Vortex Extraction

(b) Secondary Vortex Extraction

FIG. 4. Z-vorticity contour plot superimposed with (a) primary (top) and (b) secondary (bottom) vortex data extraction planes.

The Q-threshold, median filter size, and minimum minor axis length are identical for post-processing the experimental and simulation data. These values were fine-tuned based off of how much noise was observed in the detected secondary vortices. This approach was used in the joint experimental and numerical investigation from Schwarz *et al.*²¹ to quantify the development of secondary vortex structures in the wake of a two-bladed rotor out-of-ground effect. In that study, the number of secondary vortices detected in the experiment and simulation agreed well for axial positions $z/R \geq -0.6$. For this analysis, data are sampled every four time-steps (or every 1°) over a duration of five revolutions, resulting in 1800 velocity fields at each axial station. For a given axial position, the number of secondary vortices in the horizontal plane is computed at each time step. Then, the average number of

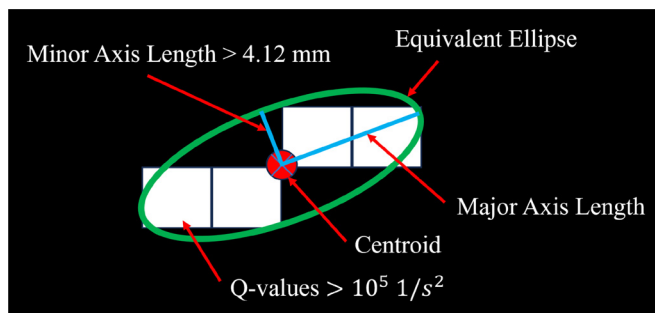


FIG. 5. Illustration of the MATLAB function “bwpropfilt” used to identify the secondary vortices.

secondary vortices per time step for each axial position is found. For the experiment and simulations, for each horizontal plane (16° extent), the average detected number of secondary vortices per time step is extrapolated to 360° azimuth.

A. Effect of sub-iteration convergence

One commonly identified vortex parameter is the swirl velocity V_θ encompassing the vortex core. In order to derive the swirl velocity V_θ , the Cartesian velocity data underwent a transformation into polar coordinates and were then decomposed into radial and azimuthal components following the approach outlined by Bauknecht *et al.*³⁵ The azimuthal velocities associated with a vortex radius r were later averaged, resulting in the calculation of a single radial V_θ profile for each vortex within the instantaneous flow fields. Based on these profiles of swirl velocity, two primary parameters were obtained. The initial parameter pertains to the circulation Γ at large distances from the vortex. To ensure the extracted circulation values were not influenced by nearby vortices, a radial distance of $r = 0.5c$ was selected for extracting the circulation. Following the approach utilized by Wolf *et al.*,³⁶ Braukmann *et al.*,³⁷ and Goerttler *et al.*,¹⁷ this value is considered an approximation for the overall vortex circulation at large radii. Using the single radial V_θ -profile, the second blade tip vortex parameter extracted is the maximum swirl velocity $V_{\theta,\max}/V_h$. Using this methodology, the circulation Γ and maximum swirl velocity $V_{\theta,\max}/V_h$ are calculated for both the measured and predicted data.

Figures 6 and 7 show the measured and predicted phase-averaged primary vortex characteristics, circulation Γ , and max swirl velocity $V_{\theta,\max}/V_h$, as the near-body (NB) and off-body (OB) solver sub-iterations increase. 5, 50, and 150 NB sub-iterations are used, which corresponds to an average global residual drop of 0.75, 1.52, and 2.08 OOM, respectively; OB sub-iterations are increased from 10 to 18 to 25, which corresponds to an average global residual drop of 1.1, 2.1, and 2.8 OOM, respectively. For clarity, only the best fit line of the phase-averaged PIV data is shown. In addition to the slight increase in maximum swirl velocity $V_{\theta,\max}/V_h$ as off-body sub-iterations increase, the primary vortex characteristics do not change significantly as the sub-iteration convergence (or sub-iterations) of both solvers increase. Although the primary vortex characteristics do not significantly change, there is a large discrepancy between the measured and predicted maximum swirl velocity $V_{\theta,\max}/V_h$. This may be due to an under-resolved vortex core and will be investigated further in the subsequent sections.

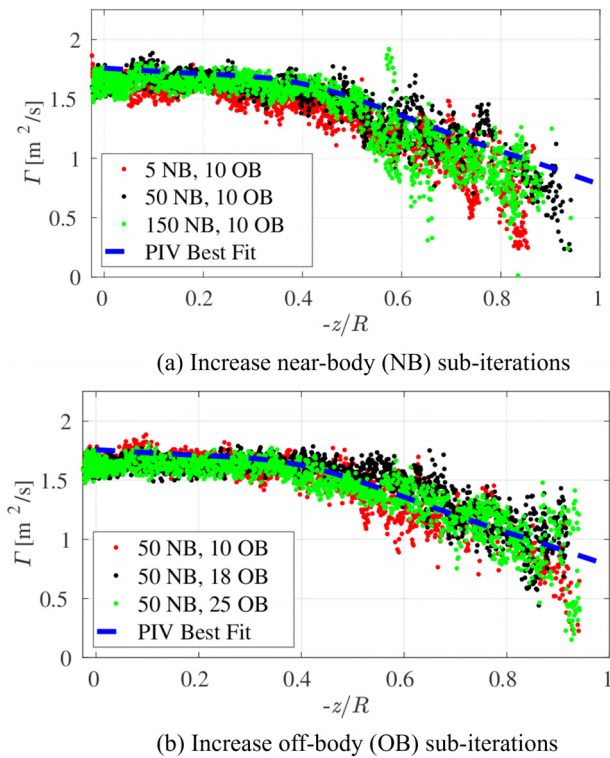


FIG. 6. Effect of increasing (a) near-body (NB) and (b) off-body (OB) sub-iterations on primary vortex circulation with the 5% simulation.

Figure 8 shows a comparison of the predicted and measured average number of secondary vortices per time step along the axial direction for the parametric sweep on NB and OB sub-iterations. As the sub-iteration convergence of both flow solvers increases, the number of secondary vortices converge. However, comparing the measured and predicted data, a large discrepancy remains for $z/R < -0.6$. This suggests there is another source of error that is causing the discrepancy in the number of secondary vortices. One hypothesis for what is causing the discrepancy is that there is a relation between the breakdown of the tip vortex and the number of secondary vortices, and therefore, if the predictions are not accurately capturing the breakdown of the tip vortex, this would lead to the discrepancy in the number of secondary vortices. In the ensuing section, the rotor thrust is varied to better understand this hypothesis.

B. Effect of thrust levels

The sensitivity of the production of secondary vortex levels is studied by varying the thrust in the simulations. Figure 9 shows the predicted tip vortex breakdown for three different thrust levels, visualized via non-dimensional Q-criterion ($\bar{Q} = 8.65$). Isosurfaces with an x-vorticity $\omega_x U_\infty / c_b$ outside the range of 3–30 have been filtered out, where x is in the longitudinal direction of the tip vortex. Comparing the three thrust levels, the primary vortex breaks down more with lower thrust. Figure 10 shows the phase-averaged tip vortex circulation as thrust is varied. The circulation plot shows that the tip vortex

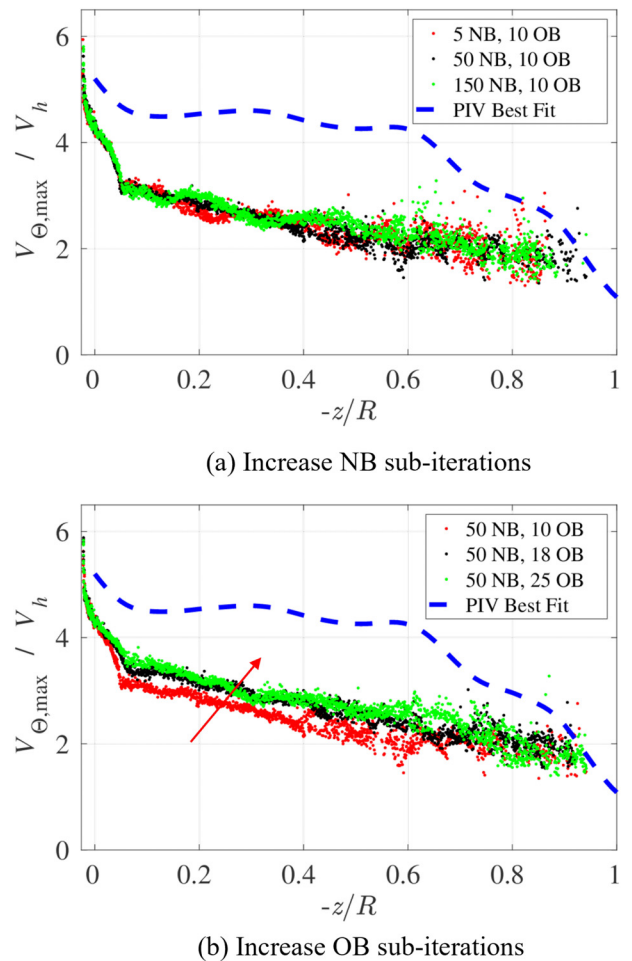
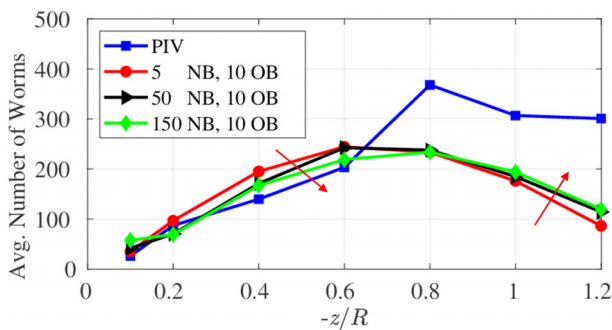


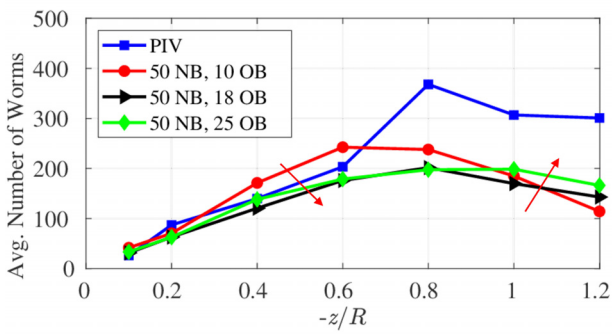
FIG. 7. Effect of increasing (a) NB and (b) OB sub-iterations on primary vortex maximum swirl velocity $V_{\theta,\max} / V_h$ with the 5% simulation.

circulation drops off more with lower thrust. Comparing the trends in Figs. 9 and 10, these results suggest that a drop in tip vortex circulation could be associated with a more broken-down tip vortex. This conclusion is important for understanding a discrepancy observed later in this paper.

Figure 11 shows a visualization of the breakdown of the tip vortex and the corresponding variation in secondary vortices for the three thrust levels; Fig. 12 shows the computed number of secondary vortices as thrust is varied. In the most downstream portion of the flow (denoted by the red box), a more broken-down primary vortex correlates with fewer secondary vortices. This demonstrates that the secondary vortex production is driven by a strong, intact primary vortex, rather than as remnants of the breakdown of the primary vortex. Since vortex pairing (observed in Schwarz *et al.*²¹) occurs in the experiment but not the simulation, this could explain the discrepancy in the number of secondary vortices in Sec. IV A. The reason for why vortex pairing occurs in the experiment but not the simulation is investigated with blade pitch angle offset in Sec. IV C.



(a) Increase NB sub-iterations



(b) Increase OB sub-iterations

FIG. 8. Effect of increasing (a) NB and (b) OB sub-iterations on average number of secondary vortices. For the experiment and simulations, for each horizontal plane, the average detected number of secondary vortices per time step is extrapolated to 360° azimuth.

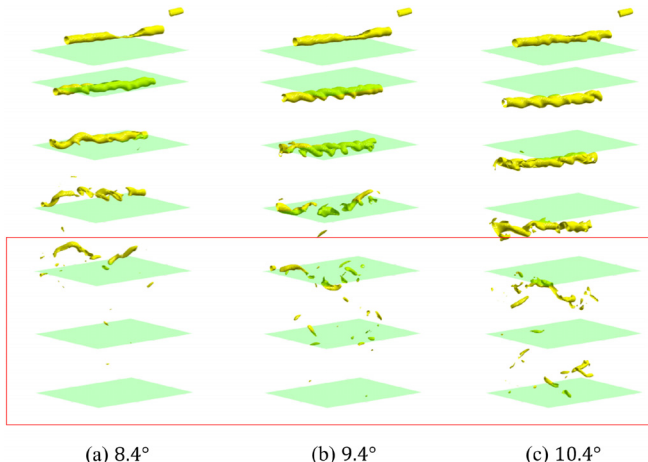


FIG. 9. Predicted tip vortex breakdown for (a) 8.4° , (b) 9.4° , and (b) 10.4° blade pitch angle, visualized via Q-criterion.

C. Effect of blade pitch angle offset

In the experiment, ideally the blade pitch angle of the two blades is set to the same exact blade pitch angle. However, measurement uncertainties and differences in the blades elastic behavior may lead to

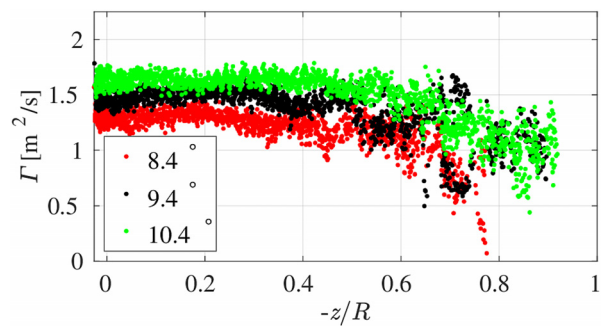


FIG. 10. Predicted phase-averaged tip vortex circulation for 8.4° , 9.4° , and 10.4° blade pitch angle.

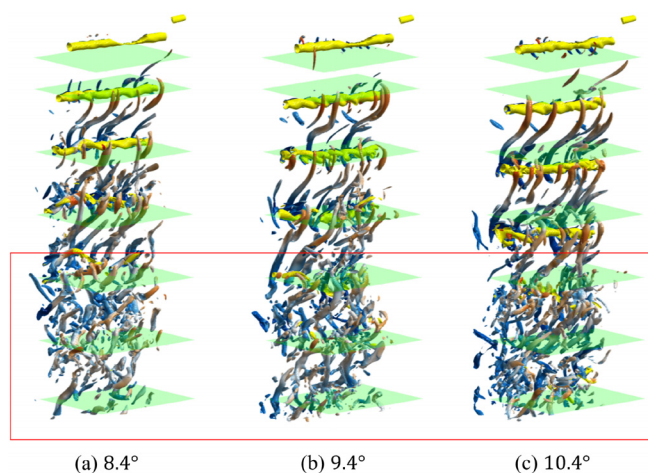


FIG. 11. Predicted breakdown of tip vortex and the associated variation in secondary vortices for (a) 8.4° , (b) 9.4° , and (c) 10.4° blade pitch angle.

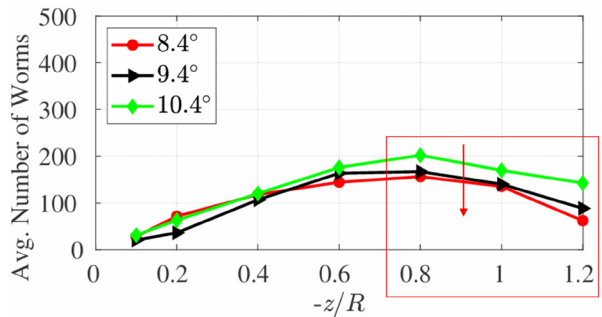


FIG. 12. Variation in predicted secondary vortices as thrust is varied via blade pitch angle.

slight offsets in the blade pitch angle between the two blades. This section models this uncertainty by intentionally using an offset in the blade pitch angle of the two blades to see whether the offset can lead to vortex pairing in the simulation; the predicted and measured number of secondary vortices is compared to see if the predictions match better

with the measurements if vortex pairing occurs. A blade pitch angle offset of 0.0° , 0.1° , and 0.5° is used. Generally, with lower numerical dissipation, the solution is more accurate as long as it remains stable. Therefore, for all three cases, as well as the remainder of this paper, the artificial dissipation coefficient is decreased from 0.04 to 0.01, which slightly decreases the number of secondary vortices for $z/R \geq -0.8$. Also, for the 0.0° offset case, the blade pitch angle is increased to 11.1° to match the measured rotor thrust. The 0.1° and 0.5° offset cases use the same blade pitch angle for blade one but a blade pitch angle of 11.2° and 11.6° , respectively, for the second blade. Figure 13 shows a comparison of the vorticity magnitude contour plots for all three blade pitch angle offset cases. The contour slice is located at the $x = 0$ plane. The phase-averaged blade tip vortex trajectory (black markers) is superimposed onto the contour plot. As shown in the plots, with no offset, there is a single vortex trajectory while with the blade pitch offset, especially with 0.5° offset, two distinct trajectories occur, which indicate the presence of vortex pairing.

Figure 14 shows how the phase-averaged tip vortex trajectory and number of secondary vortices varies as the blade pitch angle offset

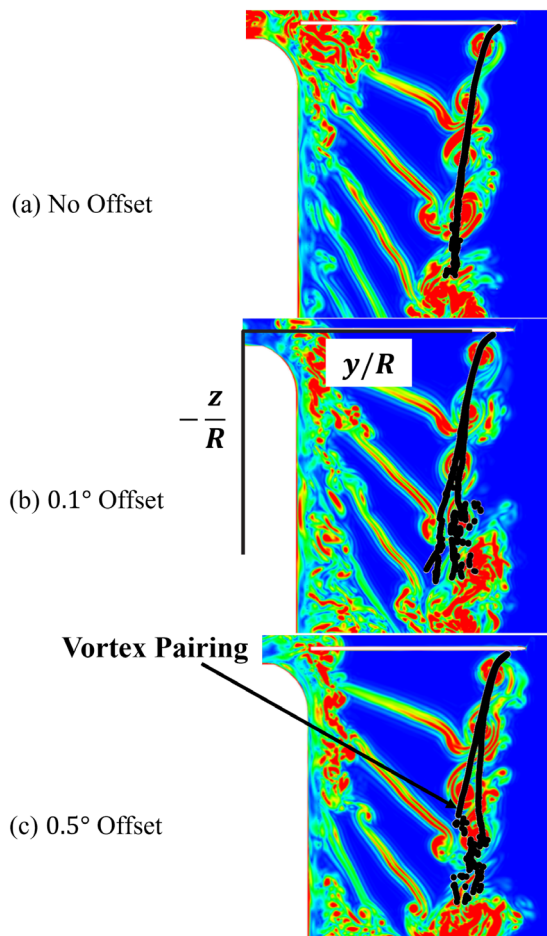


FIG. 13. Effect of blade pitch angle offset on vortex pairing is shown with vorticity magnitude contour plots for a blade pitch angle offset of (a) 0.0° , (b) 0.1° , and (c) 0.5° . Contour slice is taken at $x = 0$.

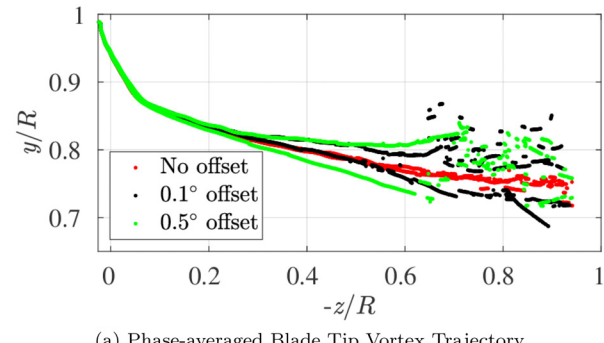
increases. Comparing the average number of secondary vortices, the peak value occurring at $z/R = -0.8$ is captured in the predictions for the 0.5° offset case, which is the case that has the most distinct vortex pairing. This demonstrates that when vortex pairing occurs in both the experiment and simulation, the decay of secondary vortices in the experiment and simulation agrees best. For 0.5° offset, the difference between experiment and simulation becomes more of a difference in the absolute number while the qualitative trend is captured correctly. As a reminder, the experimental resolution is between $1\%c$ and $4\%c$, while the current simulation grid resolution is $5\%c$. Therefore, the absolute difference in secondary vortices could be due to insufficient grid resolution in the simulation. This is investigated in Sec. IV D by increasing the grid resolution from $5\%c$ to $3\%c$.

D. Effect of grid resolution

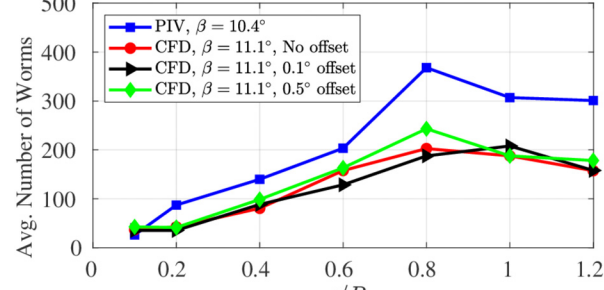
1. Comparing overall wake structure and blade tip vortices

This section seeks to understand whether the differences between the experiment and simulation are merely because of insufficient grid resolution. The grid resolution study will be done with a 0.5° blade pitch offset. A grid resolution of $\Delta x = \Delta y = \Delta z = 5\%c = 0.0021$ m and $\Delta x = \Delta y = \Delta z = 3\%c = 0.00126$ m is used.

As seen in Sec. IV C, primary vortex evolution is important for predicting the secondary vortex development. Therefore, the overall wake structure and blade tip vortices are analyzed using $5\%c$ and $3\%c$ grid resolution. Figure 15 shows a comparison of velocity (a + c) and



(a) Phase-averaged Blade Tip Vortex Trajectory



(b) Average Number of Secondary Vortices

FIG. 14. Effect of blade pitch angle offset on vortex pairing is shown with (a) phase-averaged blade tip vortex trajectory profiles and (b) the resulting average number of secondary vortices.

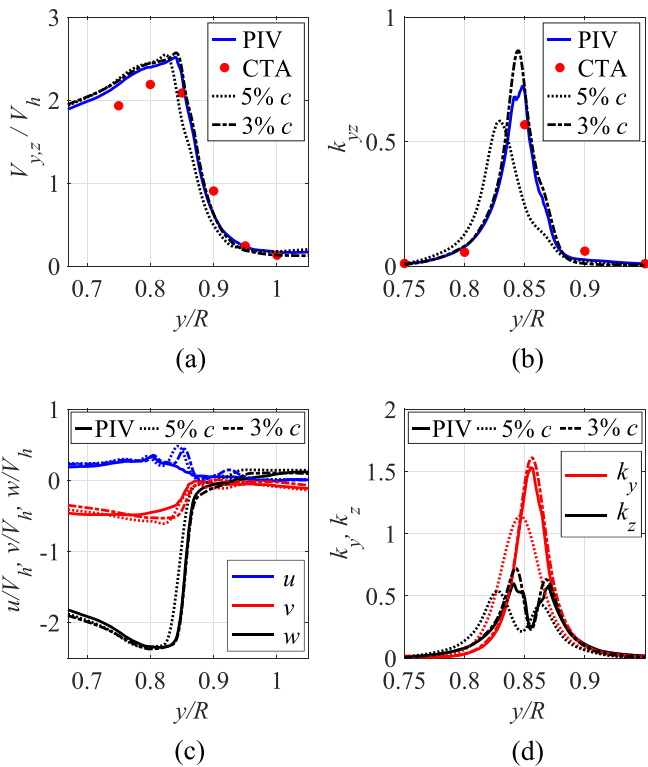


FIG. 15. Comparison of (a) and (c) velocity and (b) and (d) turbulent kinetic energy (TKE) profiles along the radial direction at an axial position of $z/R = -0.194$. Predictions are with 0.5° blade pitch angle offset.

turbulent kinetic energy (TKE) (b + d) profiles along the radial direction at an axial position of $z/R = -0.194$. Comparing the measured and predicted profiles of the two simulations, the finer resolution mesh better predicts the velocity and kinetic energy profiles. Both the magnitude and location of peak TKE is better resolved with finer resolution. The wake profiles of the finer resolution simulation also show better agreement with the experiment than the previously reported simulation in Schwarz *et al.*²¹

Figure 16 shows a comparison of the primary vortex characteristics for the experiment and the two different grid resolutions. The solid and dashed black lines are a smoothing spline fit of the data. The figure shows that swirl velocity is better predicted with the finer grid. This shows that the discrepancy in maximum swirl velocity $V_{\theta,\max}/V_h$ in Fig. 7 was due to an under-resolved vortex core. However, the circulation of the coarser grid simulation better matches with the experiment. The coarser grid circulation drops off at around $z/R = -0.6$, while the finer grid remains relatively constant. In Sec. IV B (see Fig. 10), it was observed that the circulation dropped off as the tip vortex broke down more. Therefore, this suggests that the primary vortex breaks down sooner with the 5%*c* case and the experiment. More research is needed to fully understand this discrepancy.

2. Comparing the secondary vortex development

Figure 17 shows a comparison of the measured vs predicted (5%*c* and 3%*c*) sample velocity fields at wake age of $\Psi_w = 125^\circ$ taken at a

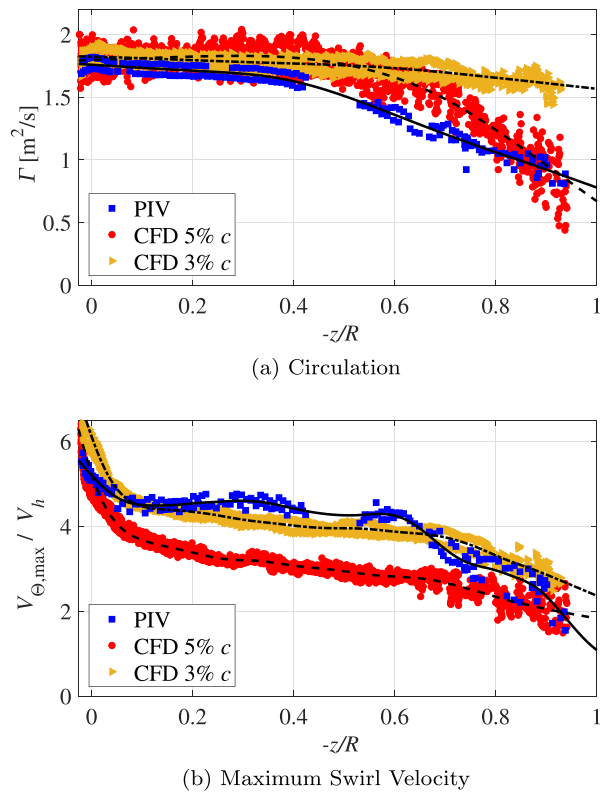


FIG. 16. (a) Phase-averaged blade tip vortex circulation Γ and (b) maximum swirl velocity $V_{\theta,\max}/V_h$ over axial position z/R . Predictions are with 0.5° blade pitch angle offset.

horizontal plane of $z/R = -0.4$. The contours represent the signed Q values after applying the filtering scheme for secondary vortex detection. The shape of the secondary vortices (in regard to vortex core size) in the finer grid simulation more closely resembles the measured secondary vortices than the coarser simulation. The secondary vortices in the finer resolution simulation also shows better agreement with the experiment than the previously reported simulation in Schwarz *et al.*²¹

Figure 18 shows the variation in predicted secondary vortices as grid resolution and sub-iteration convergence varies. A summary of the sub-iterations (SI) and global sub-iteration residual drop (RD) is shown in Table IV. Comparing 5%*c* and 3%*c* high sub-iteration convergence (red and orange lines), 3%*c* better matches the number of secondary vortices in the experiment. For the 3%*c* simulation, if using lower sub-iteration convergence (black line) there is actually more secondary vortices, which agrees less with the experiment. Bodling and Potsdam²⁰ showed that high sub-iteration convergence is required to minimize breakdown of the vortex sheet. These additional secondary vortices could be artifacts due to the vortex sheet being broken down more, which causes spurious secondary vortices. Interestingly, the 3%*c* low sub-iteration convergence case and the 5%*c* case correctly predicts the location of the peak value occurring at $z/R = -0.8$, while with the 3%*c* high sub-iteration convergence case, the number of secondary vortices continues to increase past $z/R = -0.8$. It appears this error is related to the discrepancy in circulation observed in Fig. 16, where the primary vortex was believed to break down sooner with the 5%*c* case

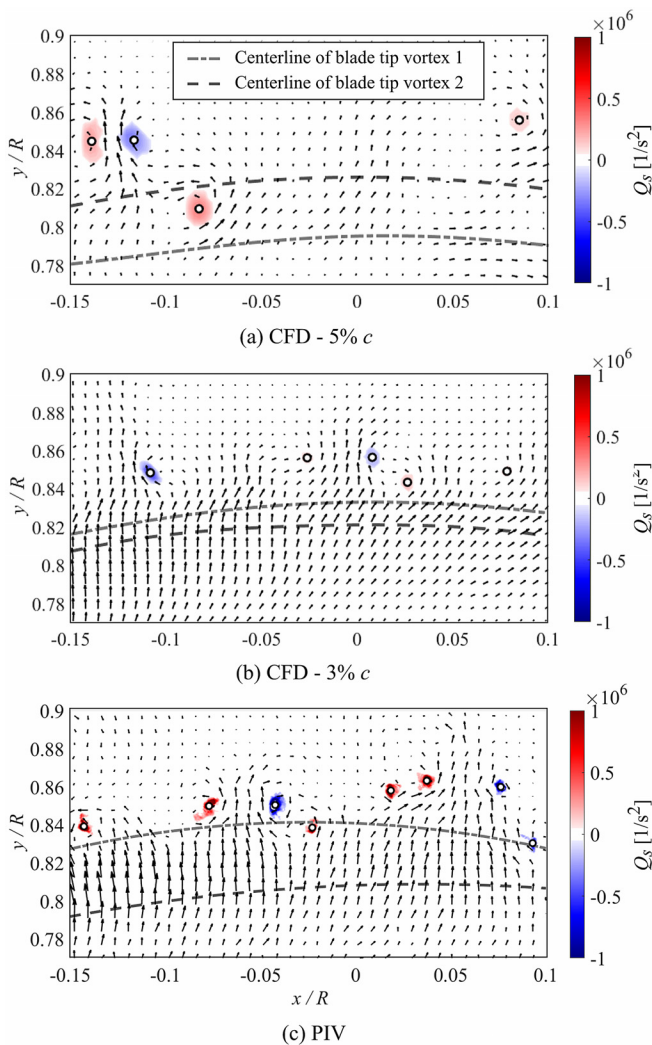


FIG. 17. Comparison of the (a) and (b) predicted ($5\%c$ and $3\%c$) vs (c) measured sample velocity fields at wake age of $\Psi_w = 125^\circ$ taken at $z/R = -0.4$. The contours represent the signed Q values after applying the filtering scheme for secondary vortex detection. Predictions are with 0.5° blade pitch angle offset.

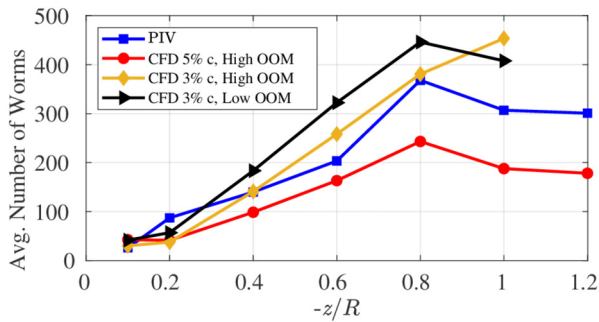


FIG. 18. Figure shows variation in predicted secondary vortices as grid resolution and sub-iteration convergence varies. Predictions are with 0.5° blade pitch angle offset.

TABLE IV. Number of sub-iterations (SI) and residual drop (RD) for high and low sub-iteration $3\%c$ cases.

| Case | OVERFLOW SI | OVERFLOW RD (OOM) | SAMCart SI | SAMCart RD (OOM) |
|---------|-------------|-------------------|------------|------------------|
| High SI | 100 | 0.97 | 27 | 2.0 |
| Low SI | 60 | 0.74 | 18 | 1.3 |

than the $3\%c$ case. Higher numerical dissipation due to low sub-iteration convergence or insufficient grid resolution may artificially cause the primary vortex to break down sooner and thereby, *coincidentally* match the peak location of the experiment. This coincidence may occur if there is another source of error that is not being accounted for in the current simulations, such as inadequate turbulence modeling. The use of LES or turbulence transition models may help shed light on this discrepancy.

To better understand the effect of grid resolution, we compare the secondary vortex histograms at $z/R = -0.8$ for $5\%c$ and $3\%c$ grid resolution with high sub-iteration convergence (see Fig. 19). In the histogram, the experiment is colored in blue and the simulation is colored in red, where the first row is the $3\%c$ simulation and the second row is the $5\%c$ simulation. In the histogram plots, the peak demonstrates the maximum swirl and circulation value of most of the secondary vortices. Comparing $3\%c$ (first row) and $5\%c$ (second row) grid resolution, it appears that the $3\%c$ grid resolution simulation is qualitatively in much better agreement with the experiment regarding the distribution of the secondary vortices (for both circulation and maximum swirl velocity). However, both simulations agree with the experiment in that the predicted secondary vortices have a symmetric distribution of positive and negative circulation. In Sec. IV E, we explain the mechanism causing the symmetric distribution of positive and negative circulation.

E. Development of secondary vortices

Since the $3\%c$, high sub-iteration case agrees best with the experiment, this case is used to elucidate the development of the secondary vortices. Figures 20 and 21 show the side and isometric view, respectively, of the z-vorticity (axial axis) contour plot at wake ages $\Psi_w = 0.0^\circ, 30.0^\circ, 60.0^\circ$, and 90.0° . In the contour plot, the red and blue contours show the sense of rotation of the vortices and vortex sheet, where counterclockwise rotating is colored in red and clockwise rotating is colored in blue. The isometric view includes the Q -criterion isosurface to visualize the tip vortex. At early wake ages ($\Psi_w \leq 30^\circ$), thin alternating counterclockwise (colored red) and clockwise (colored blue) sheets of vortices are shed from the blade. From $\Psi_w = 60^\circ - 90^\circ$, the vortex sheets get entrained into the adjacent and preceding tip vortices, which stretches the vortex sheets and results in alternating counterclockwise and clockwise rotating secondary vortices. This explains why there was a symmetric distribution of positive and negative secondary vortex circulation observed in the histogram plots in Sec. IV D. CFD animations from Chaderjian¹² also indicated that the confluent boundary layers leaving the blade trailing edge, which have opposite signs of vorticity, lead to the clockwise and counterclockwise rotating secondary vortices.

Figure 22 shows the early stages of evolution of the wake vortex system spanning from 5 to 16.5 revolutions. From 5 to 13 revolutions

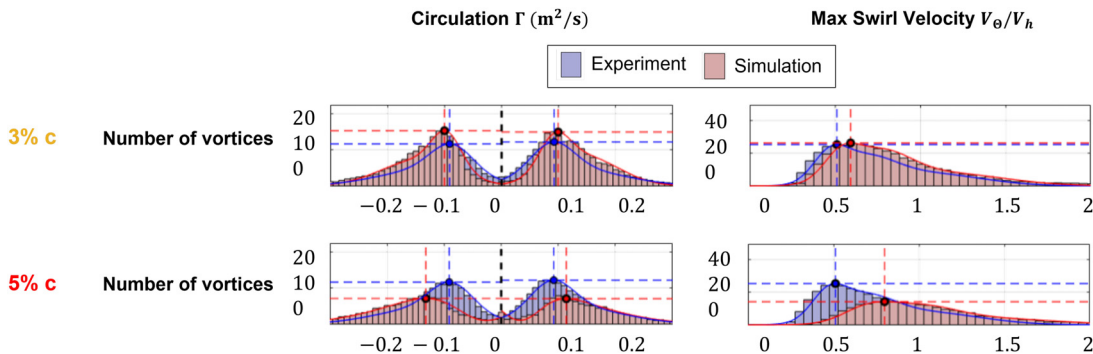


FIG. 19. Effect of grid resolution on secondary vortex histograms of maximum swirl velocity $V_{\theta,\max}/V_h$ (left column) and circulation Γ (right column) at $z/R = -0.8$.

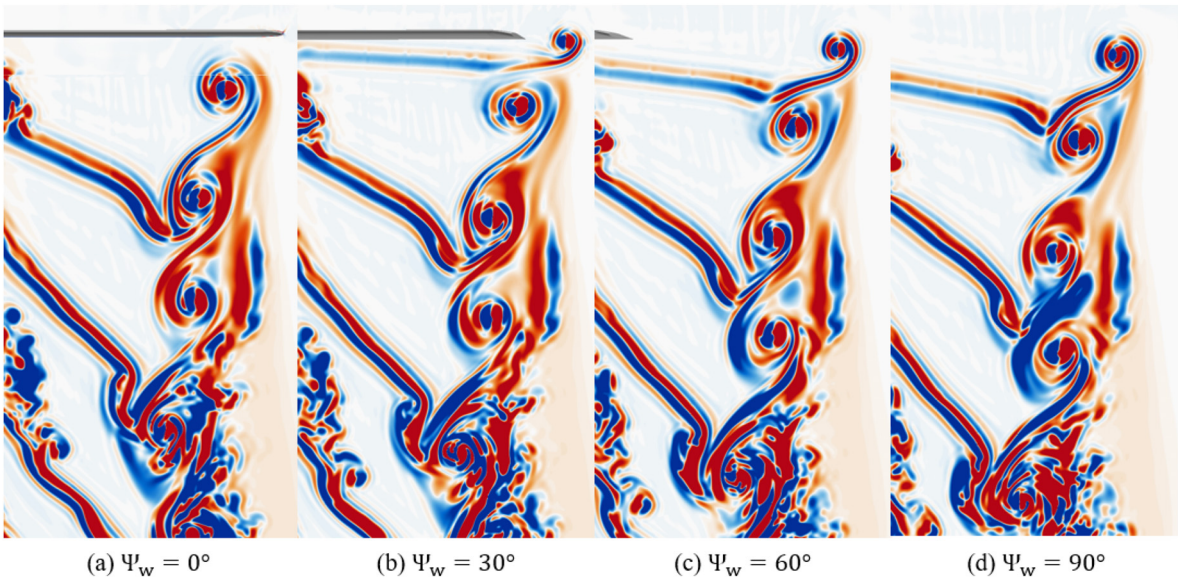


FIG. 20. Z-vorticity contour plot at wake age of Ψ_w = (a) 0.0° , (b) 30.0° , (c) 60.0° , and (d) 90.0° .

(first row), the tip vortices slowly move closer to one another. From 14.5 to 16.5 revolutions (second row), after the two tip vortices are close enough to each other, their corresponding secondary vortices that are wrapped around them collide (which are moving in opposite directions *between* the tip vortices), which causes tertiary vortices to be shed outside the mixing layer (circled in black).

Figure 23 shows the process for how the tip vortices pair and eventually decay alongside the secondary vortices. The figure spans from $\Psi_w = 0^\circ$ to $\Psi_w = 405^\circ$. Each image going from left to right is separated by 45° . For the discussion, the reader is referred to the two tip vortices within the black circles. At $\Psi_w = 0^\circ$ (top left most figure), there is a gap between the secondary vortices that are wrapped around the tip vortices. At $\Psi_w = 45^\circ$, the secondary vortices coalesce. *Between* the tip vortices, the secondary vortices are rotating about the tip vortex axis in the opposite direction (shown by arrows), and therefore, the “S-shaped” mixing layer becomes elongated (see $\Psi_w = 180^\circ$ and

$\Psi_w = 225^\circ$). From $\Psi_w = 270^\circ$ to $\Psi_w = 405^\circ$, the tip vortices are pulled into one another as they pair and as this happens, the secondary vortices twist the primary vortex which results in the eventual decay of both the primary and secondary vortices.

V. CONCLUSION

The sources of numerical error influencing the prediction of the vortex system were studied by performing high-fidelity simulations of the wake of a two-bladed rotor in hover and comparing the predictions to stereoscopic particle image velocimetry measurements in different measurement planes. Various numerical inputs, including sub-iteration convergence, blade pitch offset, and grid resolution, were varied to resolve discrepancies between the measured and predicted vortex characteristics from a previous study done by the authors. It was shown that secondary vortices impinging on structures below the rotor, which may have an impact on acoustic and vibration

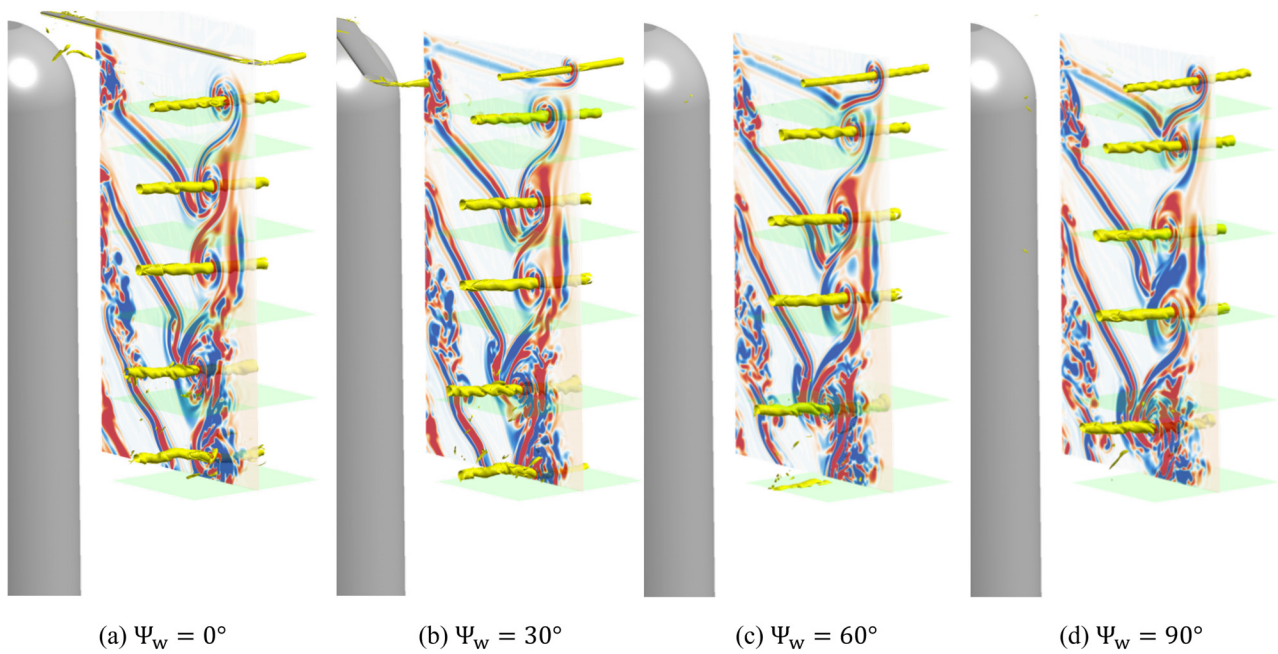


FIG. 21. Z-vorticity contour plot superimposed with Q-criterion isosurfaces at wake age of Ψ_w = (a) 0.0° , (b) 30.0° , (c) 60.0° , and (d) 90.0° .

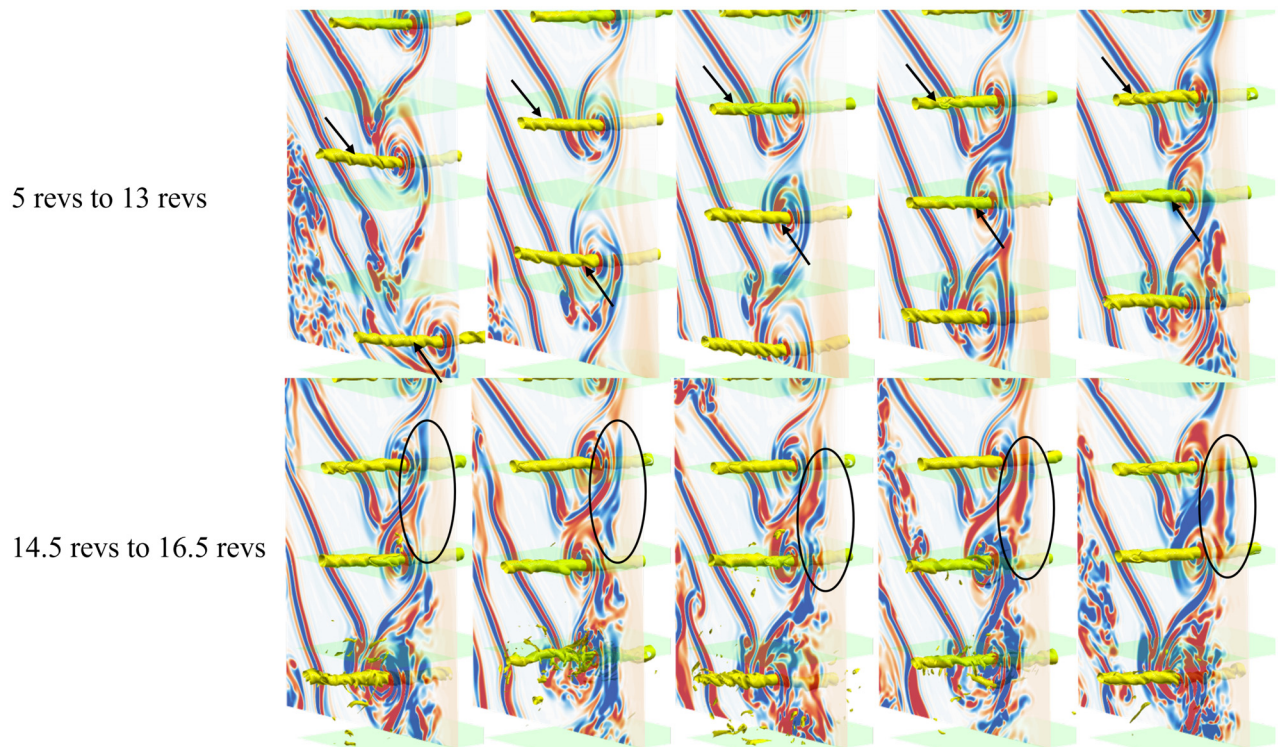


FIG. 22. Visualization of the evolution of wake vortex system.

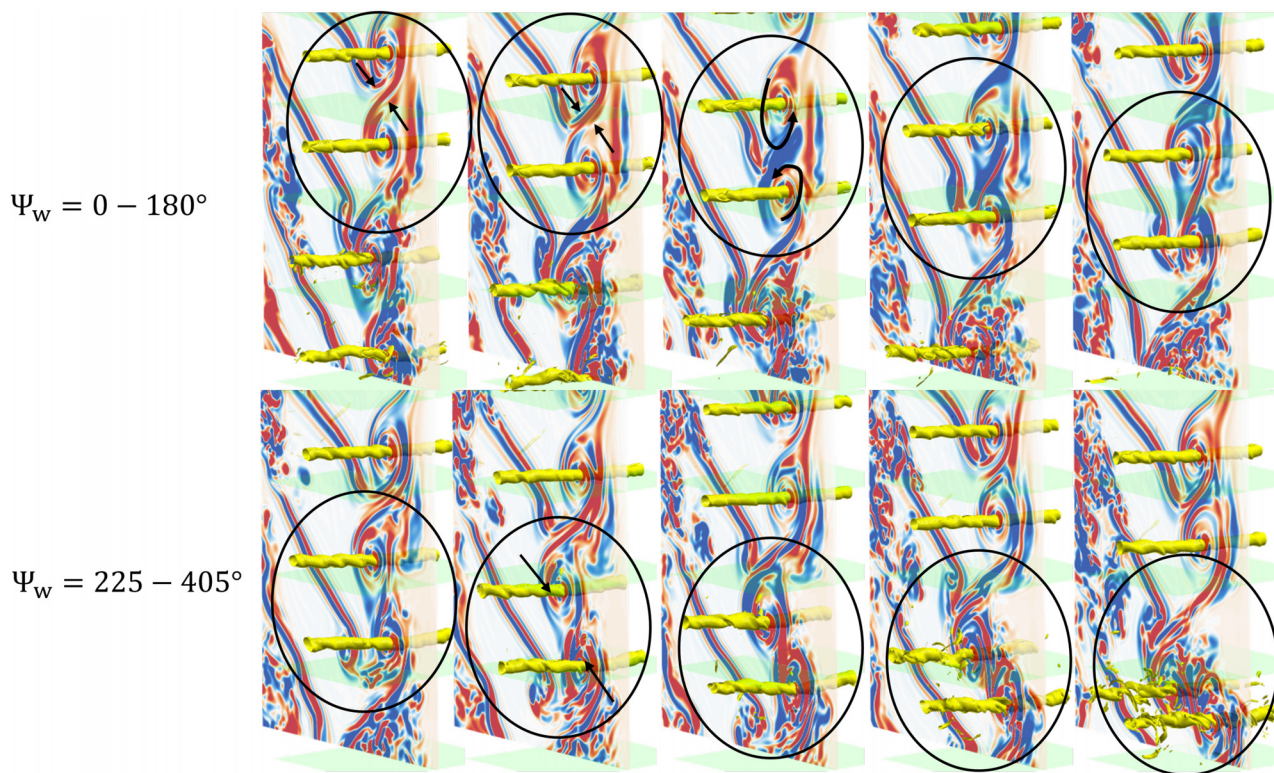


FIG. 23. The evolution of tip vortex pairing.

predictions, can be accurately predicted if the breakdown of the primary vortex is accurately captured and sufficient grid resolution/sub-iteration convergence is used. The following conclusions have been drawn from this collaborative experimental and computational study:

1. A parametric study on near- and off-body solver sub-iteration convergence demonstrated that although the secondary vortex characteristics converged as the sub-iteration convergence of both solvers increased, a large discrepancy in the number of secondary vortices remained.
2. This discrepancy was investigated by varying the thrust, where it was found that the breakdown of the primary vortex is directly linked to the number of secondary vortices.
3. Dissimilarities in the blade pitch angle, which could not be avoided in the experiment, were modeled by intentionally using an offset in the blade pitch angle of the two blades. It was shown that as blade pitch angle offset increases, vortex pairing becomes more distinct. When vortex pairing occurred in both the experiment and simulation, the decay of secondary vortices in the experiment and simulation agreed best. However, an offset in the number of secondary vortices remained.
4. To better match the experimental resolution, the grid resolution was increased from 5% chord to 3% chord, and comparing the two grid resolution simulations, the finer mesh simulation agreed best with the measured primary and secondary vortex characteristics.

5. Investigation of the development process of the secondary vortices showed that thin alternating counterclockwise and clockwise sheets of vortices are shed from the blade. The vortex sheets get entrained into the adjacent and preceding tip vortices, which stretches the vortex sheets and results in alternating counterclockwise and clockwise rotating secondary vortices. After the two tip vortices are close enough to each other, their corresponding secondary vortices that are wrapped around them collide, which causes tertiary vortices to be shed outside the mixing layer.

ACKNOWLEDGMENTS

The experimental part of the study was conducted in the framework of the DLR project “URBAN-Rescue.” The authors thank M. Krebs, J. Braukmann, A. Kostek, F. Lößle, and R. Brinkema for their help in preparing and executing the rotor tests. The simulations presented in this paper were performed using Helios, a CREATE-AV Element of the Computational Research and Engineering for Acquisition Tools and Environments (CREATE) Program sponsored by the U.S. Department of Defense HPC Modernization Program Office and U.S. Army. Computational resources provided by the DoD High Performance Computing Modernization Office, Army S/AAA Roger Strawn, are greatly appreciated.

This material is declared a work of the U.S. Government and is not subject to copyright protection in the U.S. DISTRIBUTION STATEMENT A – “Approved for public release; distribution is unlimited. PR2023496.”

AUTHOR DECLARATIONS

Conflict of Interest

The authors have no conflicts to disclose.

Author Contributions

Andrew Bodling: Conceptualization (lead); Data curation (lead); Formal analysis (lead); Investigation (lead); Methodology (lead); Software (lead); Validation (lead); Visualization (lead); Writing – original draft (lead); Writing – review & editing (lead). **Clemens Schwarz:** Conceptualization (equal); Data curation (equal); Formal analysis (equal); Investigation (equal); Methodology (equal); Software (equal); Validation (equal); Writing – review & editing (equal). **C. Christian Wolf:** Conceptualization (equal); Data curation (equal); Formal analysis (supporting); Investigation (equal); Methodology (supporting); Software (supporting); Writing – review & editing (supporting). **Anthony D. Gardner:** Funding acquisition (equal); Project administration (equal); Resources (equal); Supervision (equal); Writing – original draft (supporting); Writing – review & editing (equal).

DATA AVAILABILITY

Raw data were generated at the Department of Defense Supercomputing Resource Center (DSRC) large-scale facility. Derived data supporting the findings of this study are available from the corresponding author upon reasonable request.

REFERENCES

- ¹N. M. Chaderjian and P. Buning, “High resolution Navier-Stokes simulation of rotor wakes,” in *AHS 67th Annual Forum* (Vertical Flight Society, Virginia Beach, VA, 2011).
- ²A. Egolf, N. S. Hariharan, R. P. Narducci, and E. Reed, “AIAA standardized hover simulation: Hover performance prediction status and outstanding issues,” in *55th AIAA Aerospace Sciences Meeting, Grapevine, TX, USA* (2017).
- ³R. Jain, “A comparison of CFD hover predictions for the Sikorsky s-76 rotor,” in *AIAA SciTech 54th Aerospace Sciences Meeting* (American Institute of Aeronautics and Astronautics, San Diego, CA, 2016).
- ⁴J. Abras, N. S. Hariharan, and R. P. Narducci, “Wake breakdown of high-fidelity simulations of a rotor in hover,” in *AIAA Science and Technology Forum and Exposition, San Diego, CA, USA* (2019).
- ⁵N. S. Hariharan, J. Abras, and R. P. Narducci, “An overview of wake breakdown in high-fidelity simulations of rotor-in-hover,” in *Vertical Flight Society 75th Annual Forum, Virtual* (Vertical Flight Society, 2020).
- ⁶L. P. Bernal and A. Roshko, “Streamwise vortex structure in plane mixing layers,” *J. Fluid Mech.* **170**, 499–525 (1986).
- ⁷B. Gibeau, C. Koch, and S. Ghaemi, “Secondary instabilities in the wake of an elongated two-dimensional body with a blunt trailing edge,” *J. Fluid Mech.* **846**, 578–604 (2018).
- ⁸N. M. Chaderjian, “Advances in rotor performance and turbulent wake simulation using des and adaptive mesh refinement,” in *Seventh International Conference on Computational Fluid Dynamics (ICCFD7), Big Island, HI, United States* (2012).
- ⁹B. Lee and J. D. Baeder, “The effect of time marching on the wake structure breakdown in a hovering rotor simulation,” in *AIAA Science and Technology Forum and Exposition, Virtual* (AIAA, 2021).
- ¹⁰J. Abras and N. S. Hariharan, “Direct volume visualization for deeper insights on the physics of 3d vorticity dynamics in the wake of a hovering rotor,” in *AIAA Science and Technology Forum and Exposition, Virtual* (AIAA, 2021).
- ¹¹F. Mobley, J. Carnes, and J. G. Coder, “Modal decomposition analysis of hovering rotor wake breakdown,” in *AIAA Science and Technology Forum and Exposition, Virtual* (AIAA, 2021).
- ¹²N. M. Chaderjian, “A quantitative approach for the accurate CFD simulation of hover in turbulent flow,” *J. Am. Helicopter Soc.* **68**, 42009–42028 (2023).
- ¹³A. D. Gardner, C. C. Wolf, and M. Raffel, “Review of measurement techniques for unsteady helicopter rotor flows,” *Prog. Aerosp. Sci.* **111**, 100566 (2019).
- ¹⁴K. Kindler, K. Mulleners, H. Richard, B. G. van der Wall, and M. Raffel, “Aperiodicity in the near field of full-scale rotor blade tip vortices,” *Exp. Fluids* **50**, 1601–1610 (2011).
- ¹⁵J. G. Leishman and A. Bagai, “Fundamental studies of rotor wakes in low speed forward flight using wide-field shadowgraphy,” in *AIAA 9th Applied Aerodynamics Conference, Baltimore, MD, USA* (1991).
- ¹⁶J. N. Braukmann, A. Goerttler, C. C. Wolf, C. Schwarz, and M. Raffel, “Combining simultaneous density and velocity measurements of rotor blade tip vortices under cyclic pitch conditions,” *Exp. Fluids* **62**, 197 (2021).
- ¹⁷A. Goerttler, J. N. Braukmann, C. C. Wolf, A. D. Gardner, and M. Raffel, “Blade tip-vortices of a four-bladed rotor with axial inflow,” *J. Am. Helicopter Soc.* **65**, 1–13 (2020).
- ¹⁸R. B. Gray, *An Aerodynamic Analysis of a Single-Bladed Rotor in Hovering and Low-Speed Forward Flight as Determined From Smoke Studies of the Vorticity Distribution in the Wake* (Aeronautical Engineering Department, Princeton University, Princeton, NJ, 1956).
- ¹⁹C. C. Wolf, C. Schwarz, K. Kaufmann, A. D. Gardner, D. Michaelis, J. Bosbach, D. Schanz, and A. Schröder, “Experimental study of secondary vortex structures in a rotor wake,” *Exp. Fluids* **60**, 175 (2019).
- ²⁰A. Bodling and M. Potsdam, “Numerical investigation of secondary vortex structures in a rotor wake,” *J. Am. Helicopter Soc.* **67**, 1–18 (2022).
- ²¹C. Schwarz, A. Bodling, C. C. Wolf, R. Brinkema, M. Potsdam, and A. D. Gardner, “Development of secondary vortex structures in rotor wakes,” *Exp. Fluids* **63**, 4 (2022).
- ²²A. Heintz, C. Schwarz, C. C. Wolf, and M. Raffel, “Influence of configurational parameters on the vortex system of a rotor in hover,” in *AIAA SCITECH 2024 Forum, Orlando, Florida* (2024).
- ²³A. M. Wissink, J. Dylan, B. Jayaraman, B. Roget, V. K. Lakshminarayanan, J. Sitaraman, A. C. Bauer, J. Forsythe, and R. D. Trigg, “New capabilities in create-AV Helios version 11,” in *AIAA Science and Technology Forum and Exposition, Virtual Event* (AIAA, 2021).
- ²⁴J. Sitaraman, M. Floros, A. Wissink, and M. Potsdam, “Parallel domain connectivity algorithm for unsteady flow computations using overlapping and adaptive grids,” *J. Comput. Phys.* **229**, 4703–4723 (2010).
- ²⁵R. T. Biedron, J. Carlson, J. M. Delraga, P. A. Gnoffo, D. P. Hammond, W. T. Jones, B. Kleb, E. M. Lee-Rausch, E. Nielsen, M. Park, C. Rumsey, J. Thomas, K. B. Thompson, and W. Wood, “Fun3d manual: 13.5,” NASA 220271 (2019).
- ²⁶S. R. Allmaras, F. Johnson, and P. R. Spalart, “Modifications and clarifications for the implementation of the Spalart-Allmaras turbulence model,” in *Seventh International Conference on Computational Fluid Dynamics*, Big Island, Hawaii (2012).
- ²⁷J. Dacles-Mariani, D. Kwak, and G. Zilliac, “On numerical errors and turbulence modeling in tip vortex flow prediction,” *Int. J. Numer. Meth. Fluids* **30**, 65–82 (1999).
- ²⁸P. R. Spalart, S. Deck, M. L. Shur, K. Squires, M. K. Strelets, and A. Travin, “A new version of detached-eddy simulation, resistant to ambiguous grid densities,” *Theoret. Comput. Fluid Dyn.* **20**, 181 (2006).
- ²⁹P. Buning and R. Nichols, “User’s manual for overflow 2.3,” <https://overflow.larc.nasa.gov/home/users-manual-for-overflow-2-3/> (2023).
- ³⁰D. C. Jespersen, T. H. Pulliam, and P. Buning, “Recent enhancements to overflow,” in *35th AIAA Aerospace Sciences Meeting* (American Institute of Aeronautics and Astronautics, Reno, NV, 1997).
- ³¹M. L. Shur, M. K. Strelets, A. K. Travin, and P. R. Spalart, “Turbulence modeling in rotating and curved channels: Assessing the Spalart-Shur correction,” *AIAA J.* **38**, 784–792 (2000).
- ³²A. M. Wissink, J. Sitaraman, B. Jayaraman, B. Roget, V. K. Lakshminarayanan, M. A. Potsdam, R. Jain, A. Bauer, and R. Strawn, “Recent advancements in the

helios rotorcraft simulation code,” in *54th AIAA Aerospace Sciences Meeting* (AIAA, 2016).

³³J. I. Leffell, J. Sitaraman, V. K. Lakshminarayanan, and A. M. Wissink, “Towards efficient parallel-in-time simulation of periodic flows,” in *54th AIAA Aerospace Sciences Meeting* (AIAA, 2016).

³⁴Q. Chen, Q. Zhong, M. Qi, and X. Wang, “Comparison of vortex identification criteria for planar velocity fields in wall turbulence,” *Phys. Fluids* **27**, 085101 (2015).

³⁵A. Bauknecht, B. Ewers, O. Schneider, and M. Raffel, “Blade tip vortex measurements on actively twisted rotor blades,” *Exp. Fluids* **58**, 49 (2017).

³⁶C. C. Wolf, J. N. Braukmann, W. Stauber, T. Schwermer, and M. Raffel, “The tip vortex system of a four-bladed rotor in dynamic stall conditions,” *J. Am. Helicopter Soc.* **64**, 1 (2019).

³⁷J. N. Braukmann, C. C. Wolf, A. Goerttler, and M. Raffel, “Blade tip vortex system of a rotor with cyclic pitch,” *AIAA J.* **58**, 2869–2880 (2020).